JGR Solid Earth

RESEARCH ARTICLE
10.1029/2025JB031606

Key Points:

- Quantum Diamond Microscope discriminates between diachronous magnetizations in serpentinite throughout ophiolite history
- Mineral-scale remagnetization correlates with bulk-sample magnetic results
- Serpentinization-driven remagnetizations occur at the ridge axis and the subduction zone, with temperatures constrained by oxygen isotopes

Correspondence to:
L. Qi and Y. Zhang,
l.qi21@imperial.ac.uk;
yzhang@nigpas.ac.cn

Citation:
Qi, L., Muxworthy, A. R., Baker, E. B., Cao, X., Allerton, S., Bryson, J. F. J., & Zhang, Y. (2025). Quantifying serpentinization-driven remagnetization from ridge axis to subduction zone using quantum diamond microscopy. *Journal of Geophysical Research: Solid Earth*, *130*, e2025JB031606. https://doi.org/10.1029/2025JB031606

Received 18 MAR 2025
Accepted 2 OCT 2025

Author Contributions:
Conceptualization: Adrian R. Muxworthy, Yong Zhang
Data curation: Liang Qi, Evelyn B. Baker, James F. J. Bryson
Formal analysis: Liang Qi, Simon Allerton, Yong Zhang
Funding acquisition: Adrian R. Muxworthy, Yong Zhang
Investigation: Liang Qi, Adrian R. Muxworthy, Evelyn B. Baker, Xiaobin Cao, Simon Allerton, James F. J. Bryson, Yong Zhang
Methodology: Liang Qi, Adrian R. Muxworthy, Evelyn B. Baker, Xiaobin Cao, James F. J. Bryson, Yong Zhang
Project administration: Adrian R. Muxworthy
Resources: Liang Qi, Xiaobin Cao, James F. J. Bryson

Quantifying Serpentinization-Driven Remagnetization From Ridge Axis to Subduction Zone Using Quantum Diamond Microscopy

Liang Qi[1], Adrian R. Muxworthy[1,2], Evelyn B. Baker[3], Xiaobin Cao[4], Simon Allerton[5,6], James F. J. Bryson[3], and Yong Zhang[1,7]

[1]Department of Earth Sciences and Engineering, Imperial College London, London, UK, [2]Department of Earth Sciences, University College London, London, UK, [3]Department of Earth Sciences, University of Oxford, Oxford, UK, [4]International Center for Isotope Effects Research, School of Earth Sciences and Engineering, Nanjing University, Nanjing, China, [5]Department of Earth Sciences, Cardiff University, Cardiff, UK, [6]School of Geosciences, University of Aberdeen, Aberdeen, UK, [7]State Key Laboratory of Palaeobiology and Stratigraphy, Nanjing Institute of Geology and Palaeontology, Chinese Academy of Sciences, Nanjing, China

Abstract

Diachronous ferromagnetic (*sensu lato*) mineral populations are often juxtaposed on micrometer-to-millimeter scales. This poses significant challenges for extracting reliable paleomagnetic information because standard methods measure bulk magnetic moments and cannot distinguish between magnetic minerals with overlapping demagnetization spectra. However, the recently developed Quantum Diamond Microscope (QDM) enables micrometer-scale magnetization imaging of samples with complex remagnetization events. Here we use the QDM to quantify diachronous remagnetizations resulting from serpentinization episodes throughout the life of ophiolites, from the ridge axis where ophiolites form to the subduction zone where they are emplaced. Representative samples with contrasting bulk magnetic properties are selected from the Troodos ophiolite, Cyprus, including weakly and highly magnetic samples. QDM imaging of the weakly magnetic sample suggests that diachronous magnetizations are associated with magnetite-filled microfractures and serpentine recrystallization zones. Dipole fitting of these two zones suggests that microfracture-related magnetization corresponds to the low-field component, while serpentine recrystallization-associated magnetization corresponds to the high-field component. QDM imaging of the highly magnetic sample shows magnetic signals associated with magnetite-filled veins, carrying stable magnetization different from the weakly magnetic sample. From oldest to youngest, we interpret the highly magnetic sample as recording magnetization from ridge-axis serpentinization at 90–92 Ma. In the weakly magnetic sample, magnetization in serpentine recrystallization zones reflected mantle wedge serpentinization in the subduction zone at 2.6–5.3 Ma, while microfracture-related magnetization resulted from meteoric-water serpentinization following the surface exposure of ultramafic rocks between 0.78 and ~2.6 Ma. These different serpentinization episodes are supported by various serpentine δ^{18}O values, indicating distinct temperatures.

Plain Language Summary

Magnetic minerals in rocks can form at different times and mix, making it difficult to determine their original magnetization. Traditional methods measure the total magnetic signal of a rock but cannot separate signals from different magnetic minerals. A new tool, the Quantum Diamond Microscope (QDM), allows us to see magnetic patterns at a microscopic scale, helping untangle complex magnetization histories. This study uses QDM to investigate how rocks from the Troodos ophiolite—a piece of ancient oceanic crust—have been magnetized at different stages of their history. We examined two different serpentinites: one with weak magnetism and another with strong magnetism. The weakly magnetic serpentinite contains magnetite-filled microfractures and bulk serpentine zones. These features record different magnetic signals from separate events. The strongly magnetic serpentinite, on the other hand, has thick veins of magnetite that carry a stable magnetic signal. Our analysis reconstructs the magnetization timeline of serpentinization. The strongly magnetic sample recorded its signal during ocean crust formation (~90–92 Ma). The weakly magnetic sample acquired signals from subduction-zone serpentinization (2.6–5.3 Ma) and later meteoric water alteration (0.78–2.6 Ma). These events align with oxygen isotope variations, confirming distinct alteration temperatures.

Software: Liang Qi, Adrian R. Muxworthy, Evelyn B. Baker, James F. J. Bryson
Supervision: Adrian R. Muxworthy
Validation: Liang Qi, Adrian R. Muxworthy, Xiaobin Cao, Simon Allerton
Visualization: Liang Qi
Writing – original draft: Liang Qi
Writing – review & editing: Liang Qi, Adrian R. Muxworthy, Simon Allerton

1. Introduction

Reliable characterization of ancient magnetic fields in rocks requires the physical preservation of ferromagnetic (*sensu lato*) phases (Glenn et al., 2017). However, metamorphism, aqueous alteration and weathering are common processes that can alter these ferromagnetic minerals, leading to secondary remagnetizations (Elmore et al., 2012). Consequently, diachronous populations of ferromagnetic minerals are often found to be juxtaposed on micrometer-to-millimeter scales (Fu et al., 2020). Standard paleomagnetic techniques typically measure the net magnetic moment of whole-rock samples and cannot distinguish magnetizations carried by diachronous magnetic minerals due to overlapping demagnetization spectra (Berndt et al., 2017).

The development of mapping magnetometers, such as the quantum diamond microscope (QDM), has enabled high-resolution mapping of ferromagnetic carriers at the submillimeter scale (Fu et al., 2020; Glenn et al., 2015). The QDM is capable of isolating the remanent field on a micrometer scale, allowing for spatial correlation with the distribution of magnetic minerals within a sample (Glenn et al., 2017). The QDM has been used to measure meteorites for studying Solar Nebula magnetic fields (e.g., Fu et al., 2021; Nichols et al., 2021) and reversing Martian dynamo (Steele et al., 2023). It has also been applied in investigating terrestrial materials, including the magnetic remanence of single zircons (Fu et al., 2017; Tang et al., 2019; Weiss et al., 2018), the magnetic mineralogy of samples recording a strengthening paleomagnetic field during the late Ediacaran Period (Thallner et al., 2021), and Archean volcanic rocks, for reconstructing time-resolved lithospheric motions (Brenner et al., 2022) and seafloor hydrothermal alteration events over 3 billion years ago (Brenner et al., 2024). Here we apply the QDM to characterize chemical remagnetization resulting from serpentinization.

Serpentinization is a hydrothermal process involving the transformation of olivine and pyroxene into serpentine, brucite and magnetite, converting paramagnetic peridotite into ferromagnetic serpentinite. This process occurs throughout the life cycle of ophiolites, from the ridge axis where ophiolites are born to the subduction zone where they are emplaced (Evans et al., 2013). Investigating serpentinization in ophiolites helps elucidate the interactions between surface and deep geodynamic processes, such as the cooling mechanism near the ridge axis and the dynamics of ophiolite emplacement (Guillot et al., 2015). However, it is often challenging to identify the causes of serpentinization when more than one process is active over the tectonic history of ophiolites. For example, it is often unclear whether serpentinized rocks found in ophiolites formed during oceanic lithosphere generation at the ridge axis or through tectonic processes associated with ophiolite emplacement near subduction zones (e.g., Bonnemains et al., 2016). In this study, we present a case study in the Troodos ophiolite, Cyprus, to constrain multiple serpentinization processes from the ridge axis to the subduction zone by quantifying various chemical remagnetizations at the mineral scale using the state-of-the-art QDM, with broader implications for serpentinization studies in other regions.

2. Geological Background and Sampling

The Troodos ophiolite is considered one of the most complete ophiolites, preserving the ancient spreading axis in the Troodos region and the associated transform fault zone in its southern part (Figure 1a; MacLeod et al., 1990; Qi, Allerton et al., 2025). This ophiolite formed at 90–92 Ma in a supra-subduction zone (Gass, 1968; Mukasa & Ludden, 1987), and its emplacement onto the continent is still ongoing, experiencing geological processes ranging from the ridge axis to the subduction zone. It has undergone a 90° rotation since its formation (Clube et al., 1985; Morris, 1996), with reference paleo-directions at different ages shown in Figure 1b, which provides constraints on the timing of secondary remagnetization. In this study, we focus on the central Troodos where serpentinized ultramafic rocks are exposed, including the Artemis-Olympus zone of the mantle section and the Cumulate zone of the lower crust (Figure 1c; Wilson & Ingham, 1959).

The subcircular, faulted-bounded Artemis zone has been generally interpreted as a serpentinite diapir despite a core complex model proposed by Nuriel et al. (2009), consisting of harzburgite and lherzolite with serpentinization degrees >75% (Evans et al., 2021; McCallum, 1989). These peridotites are remnants of a fertile block from a mantle wedge situated above the zone where melts of the supra-subduction Troodos system formed. The emplacement of the Artemis serpentinite diapir also led to the surface exposure of the other ultramafic rocks in the Plio-Pleistocene (~2.6 Ma), including the upper mantle Olympus zone and the low-crustal Cumulate zone (Evans et al., 2021; Gass, 1977). The Olympus zone is characterized by refractory, clinopyroxene-poor harzburgite, which is partly serpentinized, with serpentinization ranging from 50% to 80%. The Cumulate zone is sandwiched between the crustal gabbro suite and the Olympus mantle section (Figure 1c; Thy, 1987). It comprises pyroxenite,

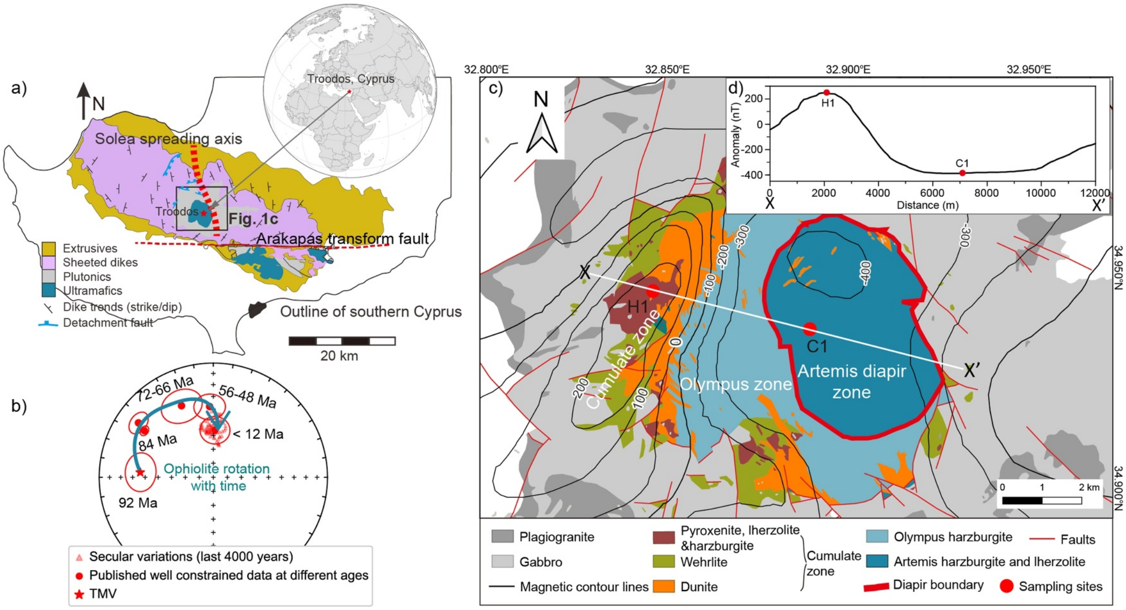

Figure 1. (a) Location and geological map of the Troodos ophiolite, Cyprus (modified after Cox et al., 2021) and (b) its rotation history, constrained by reference paleomagnetic directions from sedimentary cover of different ages (e.g., Clube et al., 1985; Morris, 1996). TMV: Troodos Mean Vector. (c) Aeromagnetic anomaly contour lines (Vine et al., 1973) and detailed geological map of the central Troodos (Wilson & Ingham, 1959). Red dots indicate the sampling localities in this study: C1 in the Artemis mantle section and H1 in the lower crust Cumulate zone. A solid red line outlines the Artemis serpentinite diapir zone. (d) Aeromagnetic profile alone XX', shows that C1 is in a negative anomaly zone, whereas H1 is in a positive anomaly zone.

dunite, wehrlite and minor amounts of harzburgite and lherzolite, formed through fractional crystallization and magmatic sedimentation (George, 1978; Greenbaum, 1972). Serpentinization in the Cumulate zone ranges from 50% to nearly complete (100%) (Qi, Muxworthy, Collier et al., 2025). It remains unclear when and how serpentinization occurred in these zones. Nuriel et al. (2009) proposed oceanic serpentinization during the ophiolite formation in the late Cretaceous; Evans et al. (2021) suggested serpentinization mainly occurred in the subduction zone after ∼5.3 Ma; Qi, Muxworthy, Collier et al. (2025) indicated that ridge axis serpentinization was primarily constrained to the Cumulate zone.

To constrain serpentinization processes in the Troodos ophiolite, we quantify serpentinization-associated remagnetization from the mineral scale to the bulk sample scale using the QDM and conventional rock and paleomagnetic techniques. Two representative sampling sites, C1 and H1, are chosen from the Artemis diapir zone and the Cumulate zone. These two sites are also representative in two contrasting aeromagnetic signals in the Troodos (Figure 1c). The Artemis-Olympus zone exhibits a negative aeromagnetic anomaly reaching −400 nT, whereas the Cumulate zone exhibits a positive anomaly reaching +280 nT (Figure 1d), measured at a survey height of 2.6 km above sea level (Vine et al., 1973). Samples from both sites were originally harzburgite but have undergone extensive serpentinization (>85–90%).

3. Methods

3.1. Rock Magnetic and Paleomagnetic Directional Analysis of Bulk Samples

To investigate the magnetic properties of our serpentinite samples, rock magnetic and paleomagnetic direction measurements were conducted at Imperial College London. High-temperature susceptibility (HT-χ) curves were measured using an AGICO MFK1-FA instrument to identify magnetic minerals. Crushed rock powders (∼500 μm) were heated from room temperature to 700°C and then cooled in Ar. Millimeter-scale rock pieces were prepared for measuring the first order reversal curves (FORCs) using a Princeton Measurements Corporation MicroMag 3900 vibrating-sample magnetometer. The field increment used for the FORC measurements is 1 mT with an applied maximum field of 0.5 T. A smoothing factor of 5 is applied during FORC data processing. Cores with a one-inch diameter and 2 cm length, were collected for demagnetization using a JR6 spinner magnetometer and an AGICO LDA-3A alternating field (AF) demagnetizer. The AF demagnetization data were analyzed using the PuffinPlot software (Lurcock & Wilson, 2012). Fisher statistics were applied to calculate mean directions (Fisher, 1953). The magnetic susceptibility of these cores was also measured using the AGICO MFK1-FA.

3.2. Scanning Electron Microscope (SEM) and Confocal Raman Microscope Analysis

Thin sections of C1 and H1 were prepared to investigate rock microstructures and magnetic minerals. Rock microstructures were examined using a Hitachi TM4000 Plus SEM, equipped with an energy-dispersive X-ray spectrometer (EDX) for elemental and compositional analysis. Mineral quantification was performed based on Raman spectra obtained with a Renishaw in Via confocal Raman microscope. Both analyses were conducted at Imperial College London. Raman analysis used a 100× dry objective (Zeiss, Oberkochen) and a 532 nm laser with a power of 50 mW (Rooney et al., 2018). Individual Raman spectrum was acquired with a step size of 366 nm and an acquisition time of 2 seconds per point. Peaks were fitted using the Gaussian-Lorentzian (Voigt) function (e.g., Yuan & Mayanovic, 2017). Obtained spectra were compared with published reference data for different minerals, including andradite (Bersani et al., 2009), magnetite (Shebanova & Lazor, 2003) and serpentine (lizardite and chrysotile) (Tarling et al., 2018).

3.3. QDM Analysis

Oriented thin sections of sample H1 and C1 with a thickness of ~30 μm were prepared for QDM measurements at the University of Oxford. This microscope, with a resolution of ~1 μm, can detect magnetization as weak as 10^{-17} Am^2 (Fu et al., 2020; Levine et al., 2019). During data collection, three orthogonal pairs of Helmholtz coils were used to cancel the local geomagnetic field and apply a uniform bias field of 900 μT to the nitrogen-vacancy layer and sample, achieving a field-nulling accuracy of approximately 0.1 μT (Glenn et al., 2017). The NRM of both samples was imaged first. Then the C1 thin section was demagnetized at 20 mT to remove the low-field component, while H1 was demagnetized at 10, 20, 35, and 60 mT. Remanent magnetizations were imaged after each demagnetization step for a specific area. The QDM data for C1 were initially processed using the QDMlab, a MATLAB toolbox (Volk et al., 2022), followed by a fast, semi-automated algorithm (Souza-Junior et al., 2024) to estimate the position and magnetization of dipolar sources. In contrast, the QDM data for H1 were processed and analyzed for the demagnetization behavior only using the QDMlab. The "globalFraction" values used were between 0.25 and 0.30. All the QDM data were applied upward continuation for 15 μm to attenuate shore short-wavelength noise (e.g., Souza-Junior et al., 2024; Volk et al., 2022).

3.4. Oxygen Isotope Analysis

To provide direct evidence for serpentinization in different tectonic settings, the ^{18}O value of serpentine was measured to estimate serpentinization temperature (Wenner & Taylor, 1971). We used the most recent geothermometer proposed by Saccocia et al. (2009): $1{,}000 \ln\alpha = [(3.49 \times 10^6)/T^2 - 9.48]$, where α is the fractionation factor between mineral and fluid, defined as: $\alpha = (1 + \delta_{\text{mineral}}/1{,}000)/(1 + \delta_{\text{fluid}}/1{,}000)$. Here, δ_{mineral} and δ_{fluid} refer to the isotopic composition in standard δ notation. All δ values are reported in units of per mil (‰) relative to VSMOW.

Given the density differences of minerals in serpentinized samples, such as relic olivine/pyroxene (~3.3 g/cm^3), magnetite (5.2 g/cm^3) and serpentine mineral (2.5–2.6 g/cm3), we applied a density filter to isolate the pure serpentine minerals using sodium Polytungstate (SPL) solution, which has a density of ~2.80 g/cm^3. During each $\delta^{18}O$ measurement, 2–3 mg of powdered serpentine sample was heated in BrF_5 gas using a CO_2 laser, facilitating fluorination and generating O_2 (e.g., Nuriel et al., 2009). The reaction products were purified using a vacuum line combined with a liquid nitrogen cold trap, followed by isolation of the purified O_2 with a molecular sieve. The purified O_2, along with reference gas, was then introduced into the MAT 253Plus mass spectrometer at the International Center for Isotope Effects Research, Nanjing University. Each sample's $\delta^{18}O$ value was averaged over three analytical runs.

4. Results

4.1. Rock Magnetic and Paleomagnetic Directional Analysis of Bulk Samples

Samples C1 and H1 are representative of contrasting bulk magnetic properties. C1 exhibits a low natural remanent magnetization (NRM) of 0.6 A/m and magnetic susceptibility of 9×10^{-3} SI, while H1 has a high NRM of 8.9 A/m

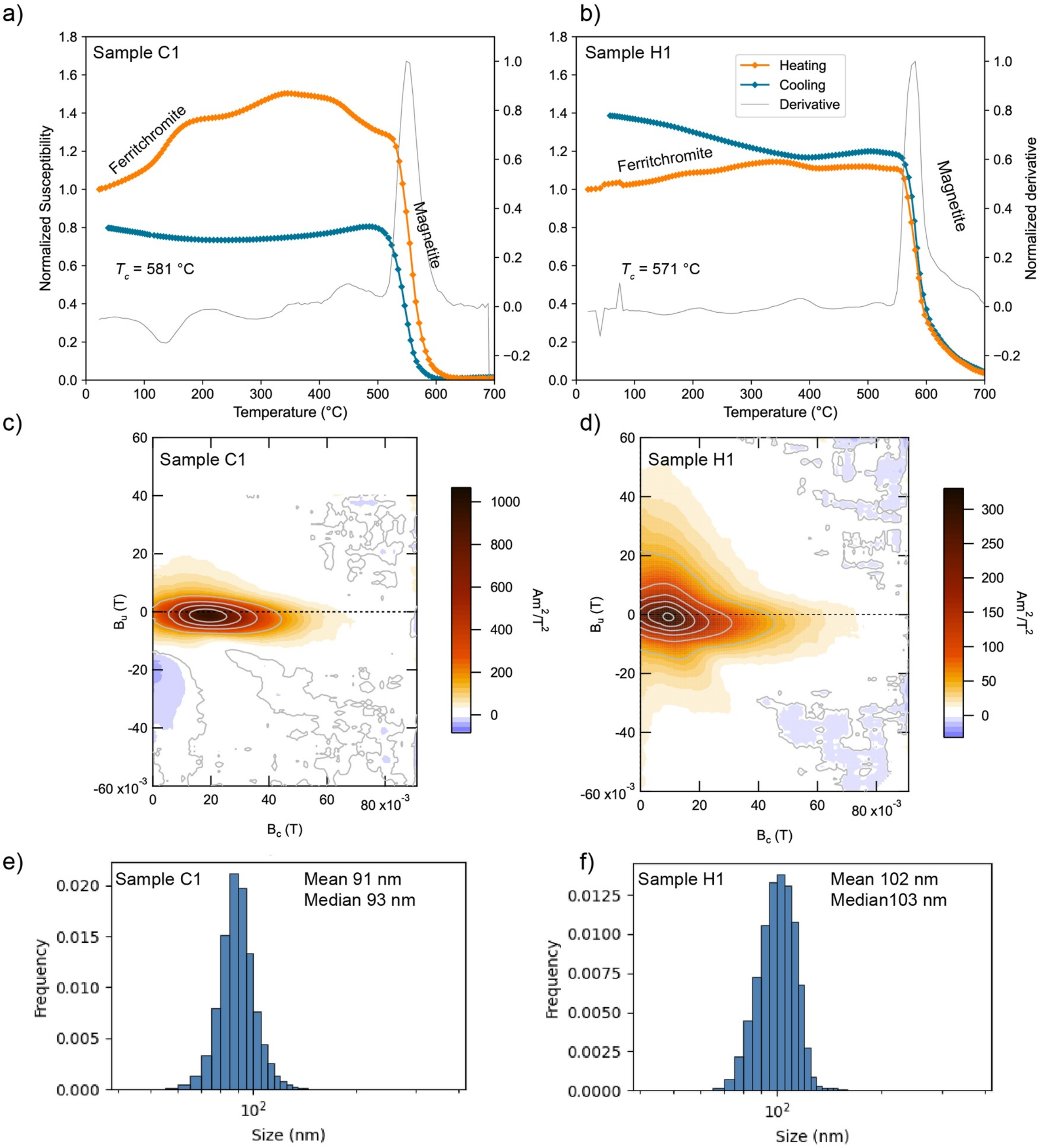

Figure 2. (a, b) HT-χ curves for C1 and H1, showing the presence of magnetic minerals, including magnetite and small amounts of ferritchromite. (c, d) FORC diagrams for C1 and H1, processed with FORCinel 3.0 using a smooth factor of 5 (Harrison & Feinberg, 2008). (e, f) Particle sizes of FORC inversion results for sample C1 and H1.

and magnetic susceptibility of 100×10^{-3} SI. This magnetic contrast is consistent with contrasting aeromagnetic anomaly zones (Figure 1c), potentially resulting from serpentinization in different tectonic settings. The dominant magnetic mineral indicated by the $HT–\chi$ curves is primarily magnetite for both sampling sites, with small amounts of ferritchromite (Figures 2a and 2b; Muxworthy et al., 2023).

The FORC diagram of Sample C1 shows a well-defined central peak aligned along the $B_u = 0$ axis, with minimal vertical spread and a relatively narrow coercivity distribution ($B_c \approx$ 20–30 mT) (Figure 2c). The peak is symmetric and strongly concentrated, with no significant vertical elongation or asymmetry. These features are characteristic of non-interacting or weakly interacting single domain (SD) particles (Roberts et al., 2000). In contrast, sample H1 displays a broader distribution in both the B_c and B_u directions (Figure 2d). The vertical spread of the peak suggests the presence of magnetostatic interactions among particles. The lack of a well-defined

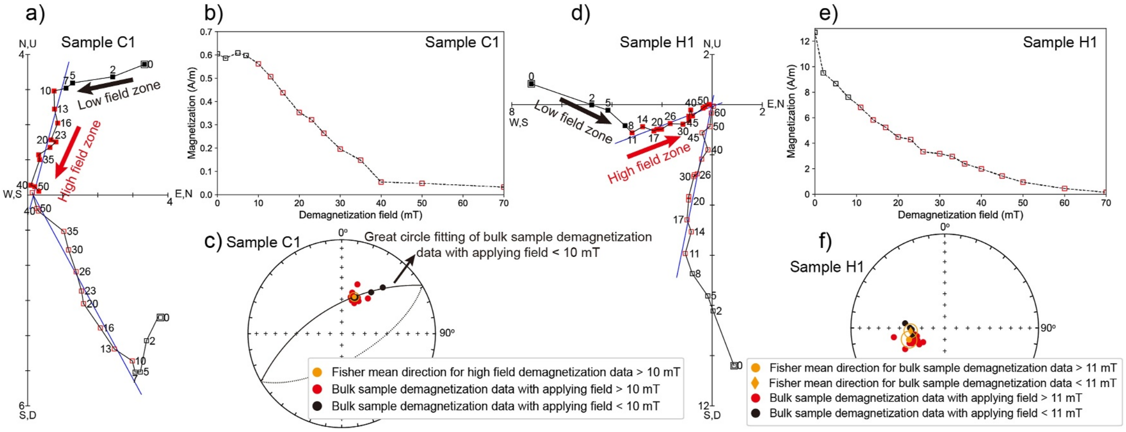

Figure 3. (a–c) Orthogonal projection plots, demagnetization curves and equal area plots for sample C1. (d–f) Orthogonal projection plots, demagnetization curves and equal area plots for sample H1. Blue lines in the orthogonal plots are PCA fitting lines in the high field zones. The great circle fitting of low field zone demagnetization data (<10 mT) for C1 is shown in panel (c). Fisher mean directions for the high field zones are also plotted.

ridge structure and the elongation in the B_u direction may indicate contributions from pseudo-single-domain (PSD) grains or clustered SD particles with significant interactions (Nagy et al., 2024; Roberts et al., 2014). To provide direct information on the magnetic grain size, we applied the latest FORC inversion tool, FORCINN, which uses a neural network algorithm to invert the size and aspect ratio distribution from measured FORC data (Pei et al., 2025). The inversion result for sample C1 shows that the frequency-normalized histogram of magnetite particle sizes exhibits a unimodal, near-symmetric distribution centered around ~90–100 nm (Figure 2e). The mean particle size is 91 nm, at the upper limit of the single-domain threshold size, but given that the particles are elongated with a mean aspect ratio of 1.70, they are likely mostly SD (e.g., Muxworthy & Williams, 2006). In contrast, the inversion result for sample H1 indicates that the magnetite particles have a mean size of 102 nm and an aspect ratio of 1.26, suggesting more PSD behavior (Figure 2f).

In the high field zone of the AF demagnetization data for the C1 sample, a Fisher mean of $D = 19°$, $I = 56°$, $\alpha_{95} = 4°$ is obtained, consistent with principal component analysis (PCA) direction of $D = 15°$, $I = 60°$ based on the Watson V test (Watson, 1983; Figures 3a–3c). However, in the low field (<10 mT), the remanent magnetization direction of C1 at each step varies on a great circle, showing the overlap of multiple components during demagnetization (Figure 3c). The high field demagnetization data (>11 mT) of H1 show a Fisher mean direction of $D = 252°$, $I = 57°$, $\alpha_{95} = 7°$, consistent with their PCA direction of $D = 249°$, $I = 60°$ (Figures 3d–3f). However, the low-field demagnetization data (<11 mT) show a Fisher mean direction of $D = 265°$, $I = 60°$, $\alpha_{95} = 6°$, inconsistent with their PCA direction of $D = 295°$, $I = 44°$, also indicating the presence of a second component in addition to the high-field one.

4.2. SEM Imaging and Raman Analysis

SEM images reveal various microstructures in C1, including microfractures, veins and serpentine recrystallization areas (Figure 4a). The microfractures cut through veins and serpentine recrystallization areas, suggesting that they are the latest structures. Some microfractures are filled with magnetite grains, indicating a microfracture-related chemical remagnetization event (Figures 4c and 4d). Few magnetite grains are found in the large serpentine veins, suggesting fluid-dominated serpentinization (Frost et al., 2013). Most of the C1 sample is characterized by serpentine recrystallization from lizardite to chrysotile (Figures 4a and 4e). Within the serpentine recrystallization area, ferritchromite is observed with grain sizes >100 μm, which is unlikely to carry stable remanent magnetization; magnetite grains are a few micrometers and are likely stable magnetic carriers (Figures 4e and 4f). The presence of paramagnetic andradite suggests that the pre-serpentinized rock of C1 likely originated in the mantle wedge zone of a subduction setting (e.g., Notini et al., 2024; Figures 4a, 4c, 4d, and 4k).

In contrast, the H1 sample is characterized by magnetite-filled veins of varying scales (Figures 4b and 4g–4j), with a much larger number of magnetite grains compared to the C1 sample. The dominant serpentine mineral is lizardite (Figures 4b and 4l). Note that the total iron oxide weight percent (FeO + Fe_2O_3) of serpentine mineral in

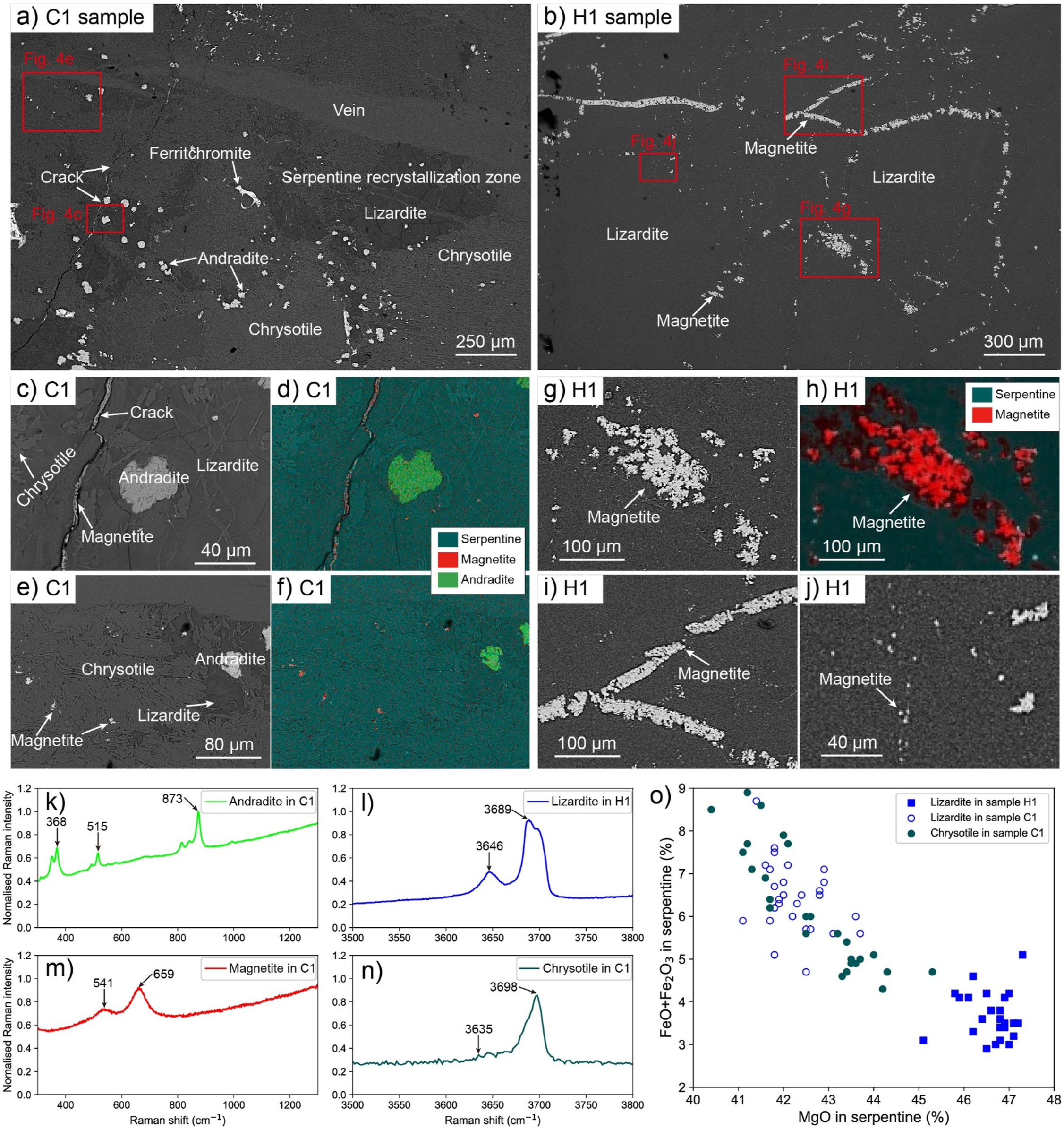

Figure 4. (a) SEM backscatter image of C1, with red boxes outlining areas of panels (c, e). (b) Backscatter image of H1, with red squares highlighting areas of panels (g, i, j). (c–f) Zoomed-in SEM images and false color maps based on EDX data, showing the magnetite-filled microfractures and serpentine recrystallization areas. (g–j) Zoomed-in SEM images and false color maps based on EDX data, showing both coarse and fine magnetite grains in sample H1, with sizes from a few micrometers to 100 μm. (k–n) Representative Raman spectra for andradite, lizardite, magnetite and chrysotile. (o) Measured oxide weight percent of iron and magnesium in serpentine minerals using the EDX point analysis, showing chemical variations between the C1 and H1.

H1 is generally between 3.0% and 4.5%, lower than that in the C1 sample, which ranges from 4.5% to 9% (Figure 4o). This iron difference suggests these two samples were serpentinized under distinct geological conditions, particularly temperature (Klein et al., 2014).

4.3. QDM Analysis

The QDM reveals different magnetic signals corresponding to the microfracture and serpentine recrystallization zones for C1 sample and magnetite-filled veins for H1 sample. Figures 5a and 5b shows the imaging results of NRM and remanent magnetization after demagnetization at 20 mT for the microfracture and serpentine recrystallization zones in C1 sample. Magnetization is carried by magnetite grains (Figures 5c–5j). Identified magnetic sources were fitted with dipole models to extract the magnetic magnitudes, declinations and inclinations (Fu

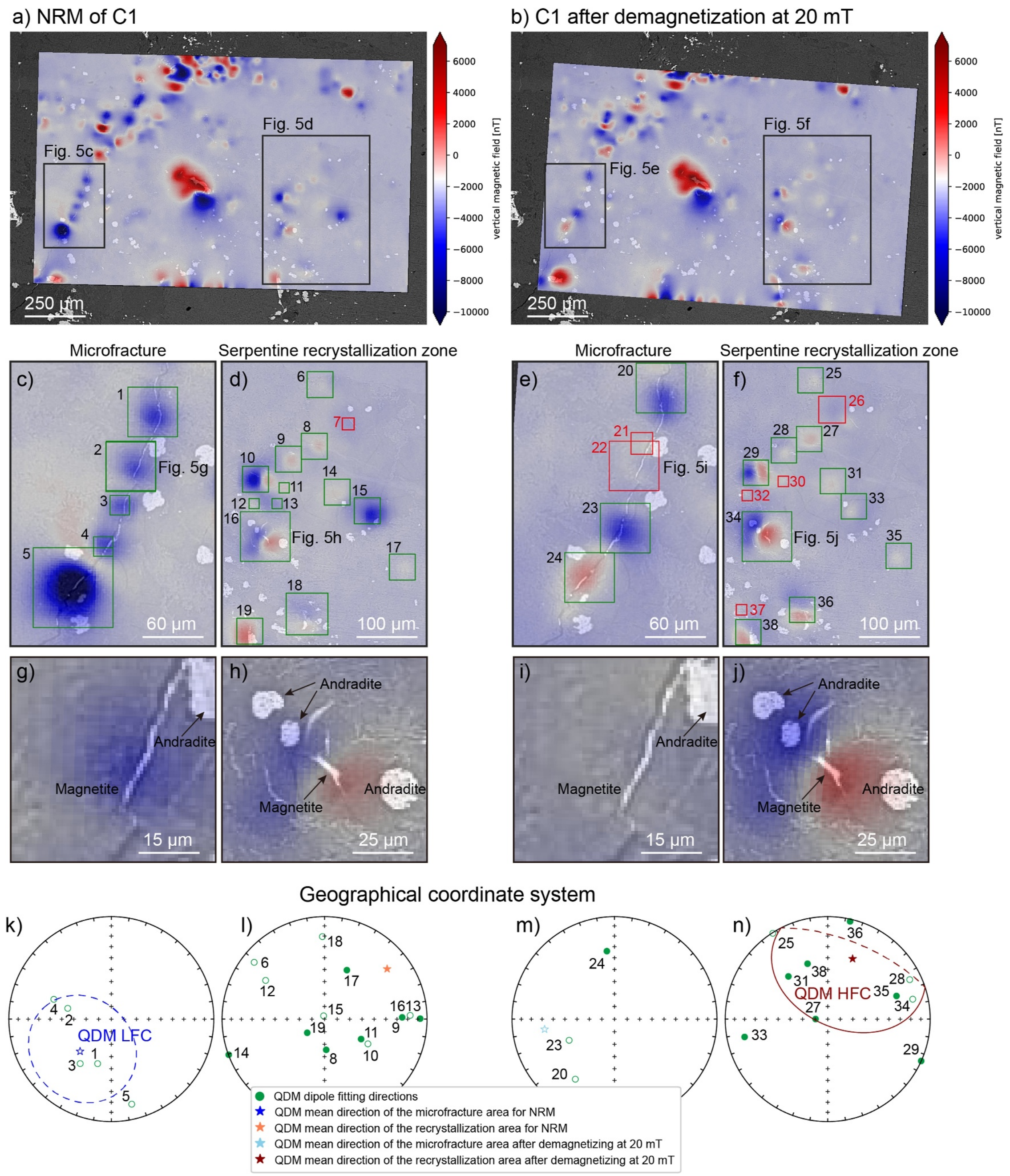

Figure 5. (a, b) QDM imaging results for the NRM and remanent magnetization after demagnetization at 20 mT for the C1 sample, overlaid on the SEM backscatter images. (c, d) Magnetic signals of NRM along the microfracture and recrystallization areas, with green squares highlighting good-fit dipole modeling sources and red boxes outlining bad-fit sources. (e, f) Magnetic signals for the same areas after demagnetization at 20 mT. (g–j) Zoomed-in images showing the correlation between magnetite grains and magnetic signals in different microstructures for sources 2, 16, 22 and 34, respectively. (k–n) Equal area plots showing directional results in the geographical coordinate system from the dipole fitting of the NRM and remanent magnetization after 20 mT demagnetization for the microfracture and recrystallization areas, with only good-fit results shown (Table 1). Mean directions for each zone with their α_{95} values are also plotted.

et al., 2020; Volk et al., 2022). Two parameters, the coefficient of determination (R^2) and signal-to-noise ratio (SNR), were calculated to evaluate the goodness of fit for the magnetic source data inversions. In this study, we applied a filter of $R^2 > 0.75$ and $SNR > 5$ to define a good fit, as suggested by Souza-Junior et al. (2024). Five dipolar sources were identified from the microfracture zone's NRM result, while 14 dipolar sources were identified for the serpentine recrystallization zone's NRM result (Figures 5c and 5d; Table 1). Dipole fitting of the five dipolar sources from the microfracture zone gave a mean direction of $D = 224°$, $I = -53°$, $\alpha_{95} = 44°$ in the

Table 1
QDM Dipole Fitting Results for the C1 Sample, Showing Mean Directions for Each Zone and Fitted Directions for Individual Dipolar Sources

				Geographical coordinate system					
Sample	Structure	Mean direction	Dipolar source number	D (°)	I (°)	M (Am^2)	R^2	SNR	Pass filter?
C1 NRM	Microfracture	$D = 224°$, $I = -53°$, $\alpha_{95} = 44°$	1	197	−53	1.90E-12	0.97	15.5	Yes
			2	284	−54	1.20E-12	0.94	12.4	Yes
			3	215	−46	8.20E-13	0.98	16.3	Yes
			4	289	−40	1.70E-12	0.99	21.4	Yes
			5	167	−16	1.60E-11	0.96	14.6	Yes
	Serpentine recrystallization zone	$D = 51°$, $I = 23°$ $\alpha_{95} > 75°$	6	309	−13	3.90E-13	0.96	14.3	Yes
			7	65	−56	1.70E-13	0.69	5.2	No
			8	177	66	3.40E-13	0.91	10.7	Yes
			9	89	25	7.50E-13	0.98	16.3	Yes
			10	120	−50	2.30E-13	0.88	9.1	Yes
			11	119	57	4.10E-13	0.93	11.8	Yes
			12	303	−32	7.80E-13	0.92	11.1	Yes
			13	90	7	1.90E-12	0.80	7.1	Yes
			14	250	0	6.20E-12	0.88	9.2	Yes
			15	344	−87	4.60E-12	0.99	19.3	Yes
			16	88	−18	2.50E-12	0.88	9.2	Yes
			17	25	46	1.70E-13	0.94	12.4	Yes
			18	359	−21	1.10E-12	0.79	6.8	Yes
			19	232	73	3.60E-12	0.81	7.4	Yes
C1 after demagnetizing at 20 mT	Microfracture	$D = 262°$, $I = -32°$, $\alpha_{95} > 75°$	20	213	−31	2.60E-12	0.96	13.9	Yes
			21	272	30	2.40E-13	0.74	5.9	No
			22	235	1	2.40E-13	0.37	2.0	No
			23	245	−50	3.70E-12	0.88	9.1	Yes
			24	354	34	3.20E-12	0.81	7.4	Yes
	Serpentine recrystallization zone	$D = 22°$, $I = 36°$, $\alpha_{95} = 58°$	25	327	−1	4.50E-13	0.96	15.0	Yes
			26	342	−53	9.50E-13	0.60	4.0	No
			27	274	80	9.70E-13	0.96	14.3	Yes
			28	64	−12	3.20E-13	0.86	9.1	Yes
			29	114	0	1.70E-12	0.94	12.2	Yes
			30	290	54	1.80E-12	0.52	3.2	No
			31	317	43	1.10E-12	0.94	12.4	Yes
			32	262	9	2.50E-13	0.45	2.7	No
			33	258	18	4.80E-13	0.87	9.3	Yes
			34	77	−16	5.90E-12	0.92	11.2	Yes
			35	71	30	2.80E-13	0.95	13.3	Yes
			36	13	2.5	2.60E-12	0.91	10.4	Yes
			37	225	−1	1.60E-13	0.69	5.2	No
			38	340	42	1.90E-12	0.79	6.8	Yes

Note. M, magnetic moment; R^2, coefficient of determination, with a maximum value of 1, that is, perfect fit of the data. SNR, signal-to-noise ratio defined in Souza-Junior et al. (2024) to evaluate fit quality. The filter applied here is $R^2 > 0.75$ and SNR > 5, which we consider as a good fit.

geographical coordinate system (Figure 5k), while dipole fitting directions of the 14 sources from the serpentine recrystallization zone, including one bad fit, were scattered (Figure 5l). After demagnetizing at 20 mT, three out of five dipolar sources for the microfracture zone were demagnetized (Figures 5i and 5m) and positive signals appeared (Figure 5e). In contrast, the dipole fitting directions for the serpentine recrystallization zone become more consistent after 20 mT demagnetization (Figure 5n). Ten good-fit dipolar sources out of 14 identified gave a mean direction of $D = 22°$ and $I = 36°$, $\alpha_{95} = 58°$ in the geographical coordinate system (Figure 5n) (Table 1). Therefore, the microfracture and the serpentine recrystallization zones record two end-member magnetic components based on the QDM results: the less stable low-field component related to the microfracture zone (QDM LFC), with direction of $D = 224°$, $I = -53°$, $\alpha_{95} = 44°$ (Figure 5k) and the more stable high-field component associated with the serpentine recrystallization zone (QDM HFC), with direction of $D = 22°$ and $I = 36°$, $\alpha_{95} = 58°$ (Figure 5n). It is worth noting that our QDM analysis is only applicable when magnetic overprints are weak and do not significantly deviate the NRM direction from the stable component. Otherwise, component fitting based on stepwise demagnetization data would be required. The QDM-derived LFC and HFC have larger α_{95} values than those obtained using the conventional paleomagnetic methods, which is expected due to the high anisotropy at the mineral scale (e.g., Berndt et al., 2016).

Unlike the C1 sample, magnetic signals are primarily associated with the magnetite-filled serpentinization veins in the H1 sample, ranging in scale from a few micrometers to hundreds of micrometers (Figures 6a–6c). Magnetite grains are closely packed, resulting in strong magnetic interactions that make it difficult to isolate the magnetic signal of individual grains. Therefore, the H1 sample is ideal for investigating the demagnetization behavior of clustered magnetite grains, rather than the dipole fitting for signal magnetite grain like C1 (Fu et al., 2020; Volk et al., 2022). We imaged magnetic signals for a specific zone using the QDM after, including the NRM and remanent magnetizations after demagnetizing at 10, 20, 35 and 60 mT (Figures 6d–6h). In this target zone, five areas were chosen, representing varying scales of magnetite veins, with area #1 being the largest and area #3 the smallest (Figures 6a–6c). By applying the demagnetization analysis method proposed by Volk et al. (2021, 2022), the QDM demagnetization data were obtained and normalized to compare with the bulk sample data, shown in Figure 6i. The QDM mean demagnetization values from these representative veins were calculated and found to be consistent with the bulk sample demagnetization (Figure 6i). This consistency suggests that these magnetite vein areas carry the characteristic remanent magnetization revealed by the bulk data of H1, that is, the stable component in the high-field demagnetization zone with a Fisher mean of $D = 252°$, $I = 57°$, $\alpha_{95} = 7°$ (Figure 3f).

4.4. Oxygen Isotope Analysis

Consistent with previously contrasting magnetic properties, the $\delta^{18}O$ values show differences between the Artemis C1 and the Cumulate H1: (a) C1 has a higher value of 9.19 ± 0.16‰ and (b) H1 has a lower value of 3.52 ± 0.10‰. This implies that the Artemis C1 was serpentinized at a relatively lower temperature than the Cumulate H1, because $^{18}O{-}^{16}O$ fractionation factor α in the serpentine-water system decreases with increasing temperature T (Wenner & Taylor, 1971; Zheng, 1993).

5. Discussion

Rock magnetic and paleomagnetic analyses clearly indicate varying magnetic susceptibility, NRM intensity and recorded paleomagnetic directions for C1 and H1 (Figure 3). SEM, EDX and Raman results highlight magnetite formations in different microstructures, such as microfractures, serpentine recrystallization zones and serpentinization fluid veins (Figure 4). Remanent magnetization was imaged using the QDM for these rock microstructures and magnetic sources identified were fitted with dipoles or investigated demagnetization behavior (Figures 5 and 6).

5.1. Understanding Dipolar Sources at the Magnetic Grain Level

Before using the QDM-derived paleomagnetic directions to investigate geological processes, it is essential to understand the origin of these dipolar signals at the magnetic grain scale, particularly for sample C1. Although there are some limitations with the FORCINN inversion of Pei et al. (2025), which is based on a numerical data set for magnetite between 45 and 400 nm and does not include any magnetostatic interactions, it still provides valuable insights into the quantitative analysis of magnetic grain sizes. We suggest that each dipolar source corresponds to a magnetite cluster with a size of a few micrometers based on SEM images (Figure 4); each cluster

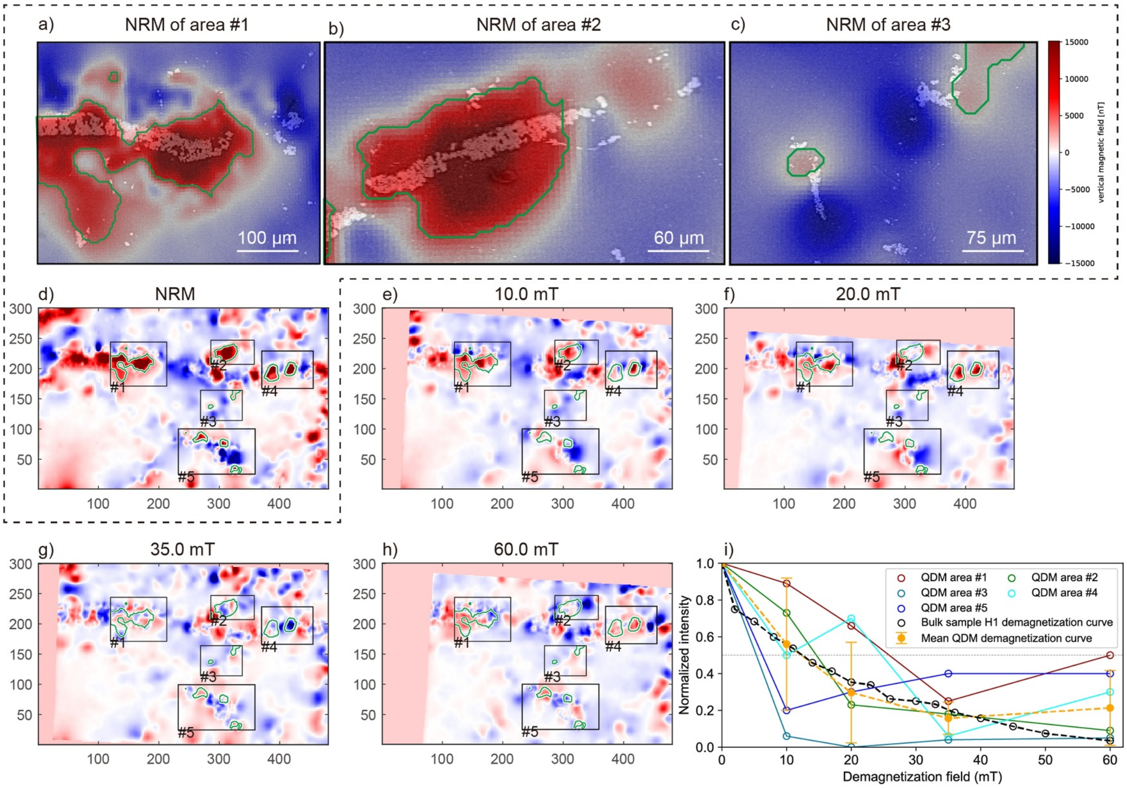

Figure 6. Demagnetization behavior of magnetite grains in H1 revealed by QDM data compared with bulk data. (a–c) QDM NRM imaging results for three areas of the H1 sample, overlaid on the SEM backscatter images. Green lines outline the main feature of positive signals. (d–h) Images of remanent magnetization after demagnetization at 0, 10, 20, 35 and 60 mT, respectively. All maps are aligned with the reference NRM mapping area. (i) Demagnetization curves for five representative areas outlined by black squares in panels (d–h), along with their mean (with 1σ error) and bulk sample demagnetization curves for comparison.

contains thousands of SD/single vortex magnetite grains with a mean size of 91 nm based on FORC inversion results in sample C1 (Figure 2e). For example, an individual SD magnetite cube with an edge length of 91 nm has a magnetic moment of $\sim 3.6 \times 10^{-16}$ Am^2, while dipolar source 1 has a magnetic moment of $\sim 1.9 \times 10^{-12}$ Am^2 (Table 1). This implies that dipolar source 1 contains ~5,000 magnetite grains. The packing fraction ϕ of the magnetite cluster can be estimated from the FORC data. The vertical half-width of the central ridge in the FORC diagram of sample C1 is $B^{\mathrm{obs}}{}_{1/2} \approx 3.8$ mT (Figure 2c). For comparison, the full-width-to-half-maximum (FWHM) of the central ridge arising from smoothing alone is $\mathrm{FWHM}_{\mathrm{smoothing}} = \delta B\,(S + 1/2) \approx 5.5$ mT, where $\delta B = 1$ mT is the field step size and $S = 5$ is the smoothing factor (Egli et al., 2010). After correction for smoothing, the intrinsic half-width is $B^{\mathrm{int}}{}_{1/2} = (2B^{\mathrm{obs}}{}_{1/2} - \mathrm{FWHM}_{\mathrm{smoothing}})/2 \approx 1.1$ mT. Using the spontaneous magnetization of magnetite, $\mu_s = 480$ kA/m, we obtain $B^{\mathrm{int}}{}_{1/2}/(\mu_0\mu_s) \approx 2 \times 10^{-3}$, where μ_0 is the magnetic permeability of free space. This corresponds to a packing fraction $\phi \approx 0.6\%$, which explains the weak magnetic interactions observed in the FORC diagram of sample C1 (Egli, 2006; Muxworthy & Williams, 2005). Additionally, the FORCINN inversion of C1 gives a mean aspect ratio of ~1.7 for the magnetite particles; the FORC data analysis based on SD physical principles yields a lower aspect ratio of ~1.2. This suggests that the particles are prolate rather than oblate, although the exact value of the aspect ratio is poorly defined.

Previous studies have examined how many grains and how large a magnetic moment a sample must have to accurately record the ambient magnetic field. Berndt et al. (2016) suggested that for samples with a thermoremanent magnetic moment greater than 10^{-11} Am^2, the assumption of a sufficiently large number of grains is generally valid. In this study, the total magnetic moments of both the microfracture zone and the serpentine recrystallization zone exceed 10^{-11} Am^2. Furthermore, a recent study by Bellon et al. (2025) indicates that in fields stronger than 10 μT, just a few thousand nanoscopic vortex-state particles can record thermoremanent magnetization with an angular error of less than 1°, regardless of particle shape. Our dipole sources include thousands of particles that satisfy these conditions, although very small and isolated SD particles might not be observed in the QDM. Therefore, it is not surprising that our dipole-fitting results for sample C1 yield reliable mean directions, that is, QDM LFC and HFC.

5.2. Serpentinization-Associated Remagnetizations From Mineral Scale to Bulk Sample Scale and Their Timing

The QDM LFC from the microfracture and HFC from the serpentine recrystallization zone in C1 sample explain the bulk sample demagnetization data. For example, the QDM HFC from the serpentine recrystallization zone is normal, comparable to the high-field bulk demagnetization data of C1 with a Fisher mean direction of $D = 19°$, $I = 56°$, $\alpha_{95} = 4°$ (Figure 7a). Both directions are comparable to the reference paleomagnetic direction of the Troodos ophiolite after the late Miocene (Figure 7a), suggesting chemical remagnetization in the serpentine recrystallization zone was acquired <12 Ma, during which the ophiolite was above the subduction zone (Clube et al., 1985). Note that both the QDM HFC and LFC are closely aligned on the fitting great circle of bulk sample demagnetization data below 10 mT (Figure 7a), suggesting that the overlapping of the two components, QDM LFC and HFC, explains the low-field bulk demagnetization data of C1. The timing for QDM LFC from the microfracture zone is later than the QDM HFC from the serpentine recrystallization zone since the microfracture cut through the serpentine recrystallization zone. Importantly, microfractures represent brittle deformation and occur only at shallow depths, forming when mantle rocks have been uplifted. The uplift and surface exposure of Troodos ultramafic rocks is generally suggested to result from diapiric emplacement in the Plio-Pleistocene (~2.6 Ma) (Evans et al., 2021; Gass, 1977). The reversed QDM LFC from the microfracture zone acquired before 0.78 Ma, that is, the Brunhes-Matuyama reversal (e.g., Bassinot et al., 1994). Therefore, we suggest that microfracture-related QDM LFC was due to serpentinization between ~0.78–2.6 Ma, after the surface exposure of serpentinized Troodos ultramafic rocks.

The QDM demagnetization behavior suggests magnetite-filled veins in H1 carry stable chemical remanent magnetization (CRM) (>10 mT), which has a Fisher mean of $D = 252°$, $I = 57°$, $\alpha_{95} = 7°$ indicated by the bulk sample demagnetization data (Figure 7b), different from any components in C1. This stable direction was suggested to be originally the Cretaceous Troodos Mean Vector (TMV) of $D = 274°$, $I = 36°$, $\alpha_{95} = 12°$ (Clube et al., 1985), but it has experienced later tectonic tilting with the seafloor spreading and development of detachment faults along the spreading ridge (Figure 7b; Granot et al., 2006; Qi, Muxworthy, Collier et al., 2025). The low-field (<10 mT) demagnetization data of H1, which slightly deviate from the stable component, might be affected by viscous remanent magnetization in the present field.

5.3. Serpentinization Temperatures From Low (<200°C) to High (>200°C)

Serpentinization temperatures estimated by the most recent $\delta^{18}O$ geothermometer proposed by Saccocia et al. (2009), suggest a lower temperature of 159 ± 2°C for C1 and a higher temperature of 245 ± 2°C for H1 (Figure 8a). The lower temperature C1 has a relatively lower magnetic susceptibility of 9×10^{-3} SI, similar to published data set of serpentinite from subduction zone with serpentinization temperature typically <200°C (Figure 8b; Bonnemains et al., 2016; Klein et al., 2014). In contrast, the higher temperature H1 has a higher magnetic susceptibility of 100×10^{-3} SI, comparable to published data set of serpentinite from the ridge-axis serpentinization with temperature >200°C (Figure 8b; Barnes et al., 2009; Klein et al., 2014). Our results are consistent with the current understanding that iron favors forming magnetite rather than iron-rich serpentine at temperature >200°C (Figure 4o; Evans, 2008; Klein et al., 2014). Note that the serpentinization temperature estimates assume that the fluid source is seawater, that is, $\delta^{18}O_{\mathrm{fluid}} = 0‰$. Since C1 sample likely forms from slab-derived fluid in the subduction zone, with $\delta^{18}O_{\mathrm{fluid}}$ generally <0‰ (Barnicoat & Cartwright, 1995), the estimated 159 ± 2°C represents the highest temperature the C1 serpentinization can reach.

5.4. Serpentinization-Related Remagnetizations From the Ridge Axis to the Subduction Zone

Before we have identified the acquisition of serpentinization-associated CRMs at varying ages, from old to young, including: (a) a strong CRM along the magnetite-filled veins in sample H1 acquired in the late Cretaceous (90–92 Ma), (b) a CRM in the serpentine recrystallization zone of C1 acquired <12 Ma in the subduction zone and (c) a CRM along the microfracture in the C1 sample acquired most likely between 0.78 and 2.6 Ma after the surface exposure of ultramafic rocks (Figure 7). Moreover, serpentinization temperatures estimated by the $\delta^{18}O$

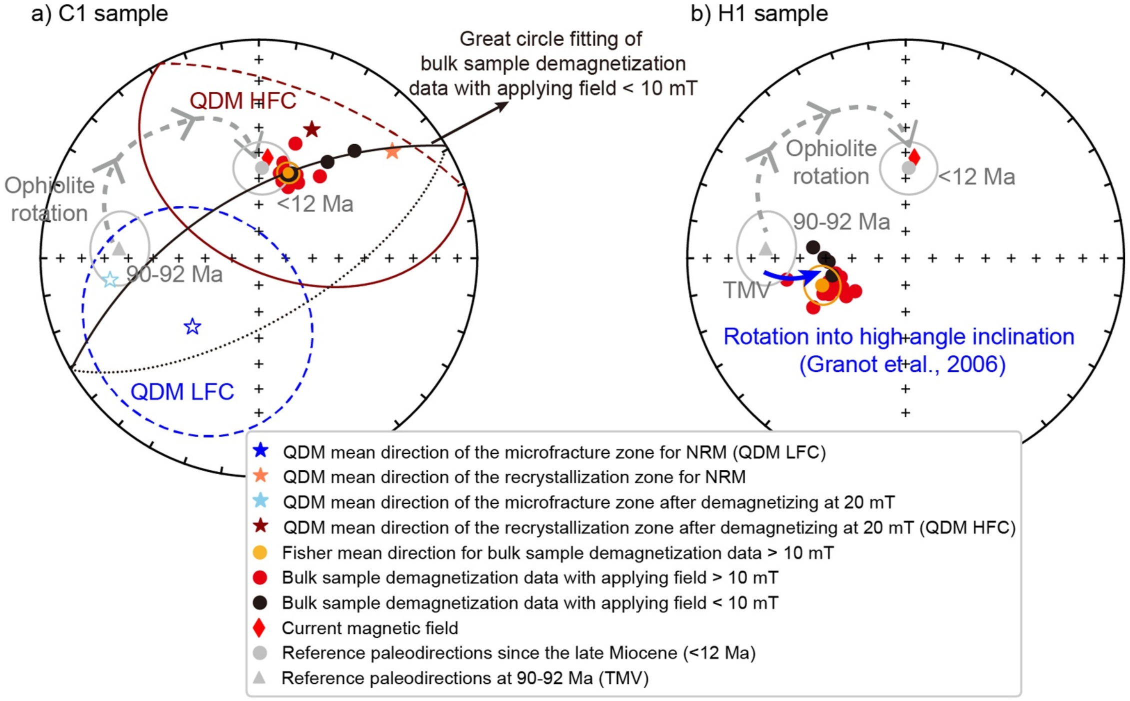

Figure 7. (a) Equal area plot showing mean directions from QDM results in comparison with the directions from standard bulk sample measurements in the geographical coordinate system for C1 sample. QDM LFC, QDM low field component related to the microfracture. QDM HFC, QDM high field component in the recrystallization zone. Rotation history for the Troodos ophiolite is also shown (Clube et al., 1985; Morris, 1996). (b) Equal area plot showing the directions from standard bulk sample measurements in the geographical coordinate system for H1 sample. Stable magnetic component (>10 mT) is carried by the magnetite-filled veins based on the QDM demagnetization results of H1.

geothermometer suggest a higher temperature of 245 ± 2°C for H1 than that of 159 ± 2°C for C1, implying different tectonic settings during serpentinization (Figure 8).

We suggest that the CRM related to magnetite-filled veins in H1 resulted from high-temperature serpentinization near the spreading axis during ophiolite formation. For example, Hurst et al. (1994) and Qi, Muxworthy, Collier et al. (2025) suggest a seafloor faulting system developed in the late Cretaceous (90–92 Ma), extending into the lower crust to accommodate the extension of the oceanic crust near the Solea ridge axis (Figure 9a). The extensional faulting allowed hydrothermal seawater to circulate into the lower crust Cumulate zone, causing serpentinization and magnetization in the TMV field. The serpentinization might be up to ~245°C based on our study. The Cumulate zone was then tilted to a steep angle due to continuous extensional forces and block rotations near the spreading axis (Figure 7b; Granot et al., 2006; Qi, Muxworthy, Collier et al., 2025). Importantly, geological evidence does not support an open system with ultramafic rocks exposed at the seabed during this time (Figure 9a), as no ultramafic sediments were preserved in the surrounding basins of Troodos before the Pleistocene (McCallum, 1989; Poole & Robertson, 1998).

Chemical remagnetization in the serpentine recrystallization zone of C1 was associated with the serpentinization event in the Troodos mantle wedge zone <12 Ma, due to released fluids from the subducted plate. This remagnetization event likely happened between 2.6 and 5.3 Ma because it was suggested that the Pliocene collision of the Eratosthenes continental block with the Cyprus trench halted the northward subduction of the African plate in the early Pliocene, causing focused fluid upwelling into the mantle sequence and initiating serpentinization (Robertson, 1998; Figure 9b). The depth of serpentinization, estimated at up to 15 km in the mantle wedge zone, is supported by seismic studies (Merry, 2022) and gravity modeling (Gass & Masson-Smith, 1963; Shelton, 1993). The serpentinization temperature is ~159°C based on our δ^{18}O analysis.

CRM acquisition along the brittle microfractures, like those in the C1 sample, was due to meteoric water serpentinization after the surface exposure of the ultramafic rocks (Figure 9c). It was proposed by Evans et al. (2021) that the serpentinized Troodos mantle wedge rocks became low-density and unstable, leading to their

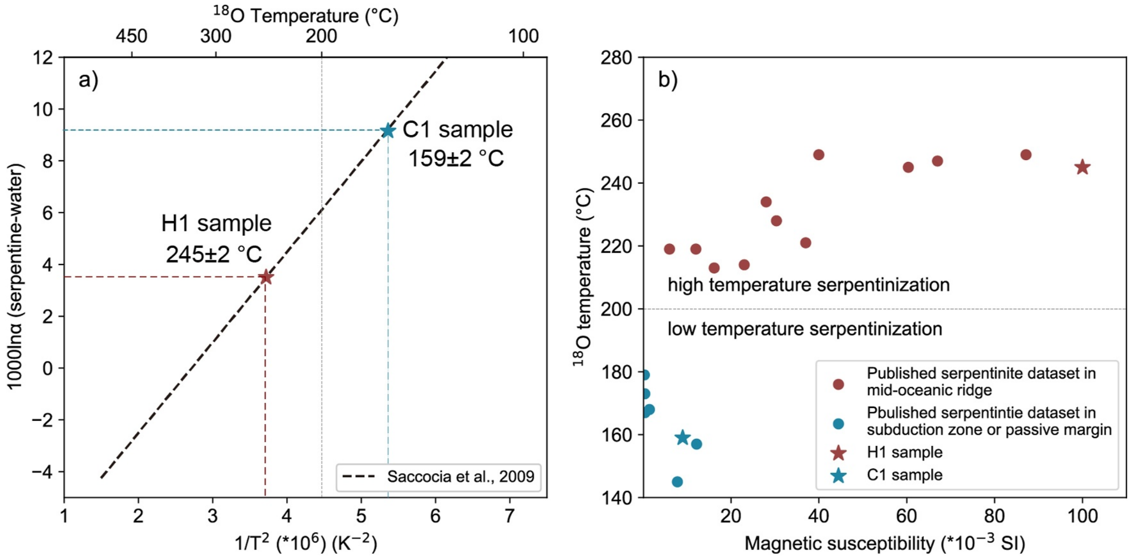

Figure 8. (a) Predicted ^{18}O−^{16}O fractionation factor α in the serpentine-water system as a function of temperature T, based on Saccocia et al. (2009). The serpentinization temperature for C1 is estimated at 159 ± 2°C, while the temperature for H1 is 245 ± 2°C. (b) Magnetic susceptibility of serpentinite against ^{18}O temperature using the geothermometer proposed in Saccocia et al. (2009). Data sets from our study and previously published studies from the mid-ocean ridge (Agrinier & Cannat, 1997; Barnes et al., 2009; Früh-Green et al., 1996; Klein et al., 2014) and subduction zone/passive margin (Klein et al., 2014; Skelton & Valley, 2000) are shown.

emplacement as a serpentinite diapir at ~2.6 Ma (Poole & Robertson, 1998), thus forming the Artemis Zone. The Artemis diapir also led to the surface exposure of the highly magnetic Cumulate and less serpentinized Olympus zones. Differential uplift between the Artemis and Olympus zones occurred due to mantle rocks with varying serpentinization degrees and densities (Figure 9c; Evans et al., 2021). With the surface exposure of those serpentinized rocks, meteoric water serpentinization occurred, with the temperature at ~25–50°C (Nuriel et al., 2009). Such meteoric water-associated serpentinization may still be occurring in some areas of the Troodos (Evans et al., 2024; Qi, Muxworthy, Collier et al., 2025).

6. Conclusions

We quantify mineral-scale remagnetizations in serpentinite using the QDM, which cannot be isolated by standard paleomagnetic and rock magnetic methods. These serpentinization-driven remagnetizations occur throughout the ophiolite history from the ridge axis to the subduction zone. Representative serpentinite samples are chosen from the Troodos ophiolite with contrasting magnetic properties, including magnetic susceptibility, NRM, magnetic grain sizes (Figure 2) and paleomagnetic directions (Figure 3). Several microstructures with the presence of magnetite are found in these samples, including microfractures, serpentine recrystallization zones and serpentinization veins (Figure 4). Corresponding to these microstructures, our study identifies three episodes of serpentinization-associated chemical remagnetization, as indicated by the QDM results and the magnetic properties of bulk samples (Figures 5–7). These episodes are, from oldest to youngest: (a) CRM acquisition due to high-temperature ridge-axis serpentinization at 90–92 Ma in the Cumulate H1 sample, (b) CRM acquired in the Artemis C1 sample during serpentinization of the ophiolite mantle in the subduction zone (<12 Ma), most likely between 2.6 and 5.3 Ma, and (c) meteoric water-related serpentinization following the surface exposure of Troodos ultramafic rocks, which led to chemical remagnetization along microfractures in C1 between ~0.78 and 2.6 Ma. These processes in different tectonic settings are supported by δ^{18}O-derived serpentinization temperatures, with a higher temperature of 245 ± 2°C for the ridge axis serpentinization than 159 ± 2°C for the subduction zone serpentinization and below 50°C for meteoric water serpentinization.

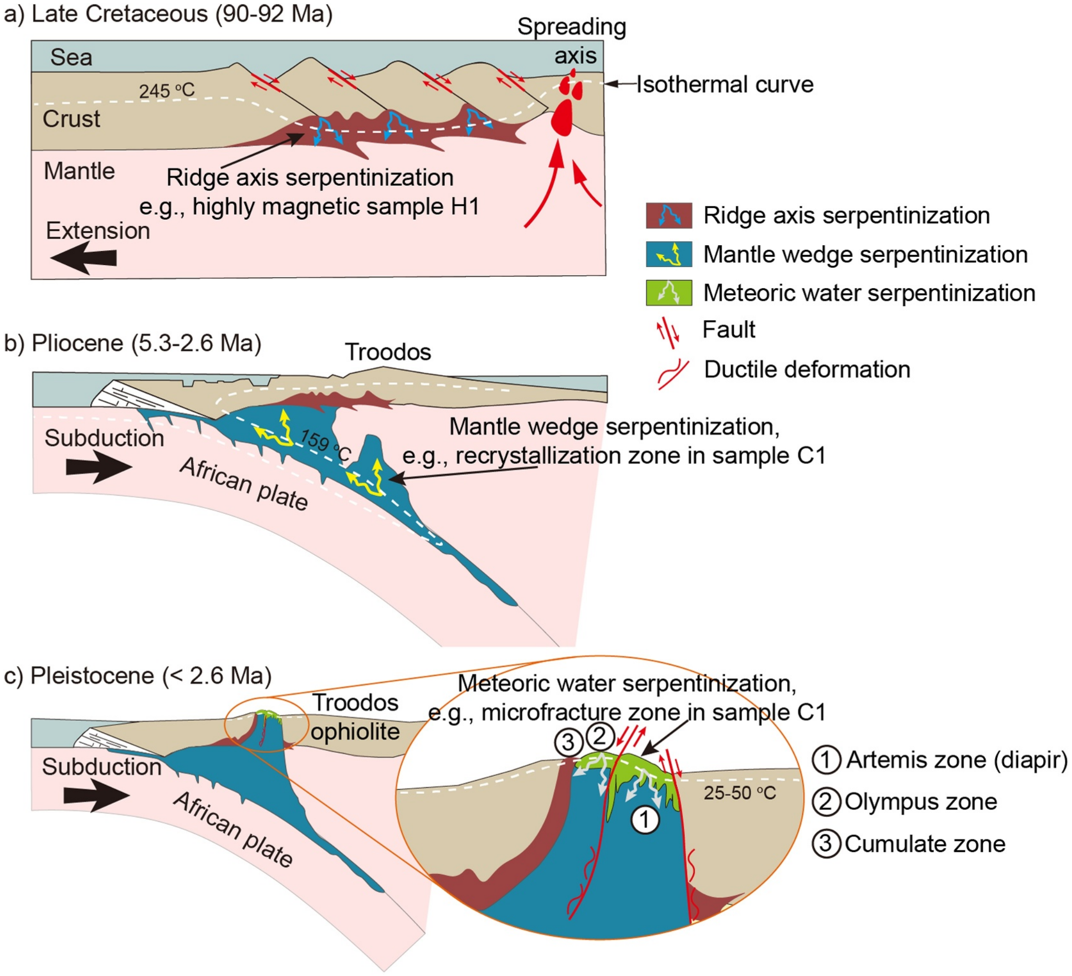

Figure 9. Three stages of serpentinization processes. (a) Ridge-axis serpentinization during ophiolite formation, leading to highly magnetic serpentinite, for example, sample H1. (b) Mantle wedge serpentinization in the subduction zone, characterized by the serpentine recrystallization zone in sample C1. (c) Meteoric water serpentinization, giving rise to the microfracture-related magnetization after surface exposure of the ultramafic rocks.

Conflict of Interest

The authors declare no conflicts of interest relevant to this study.

Acknowledgments
L.Q. thanks the British Geophysical Association for the Gray-Milne Travel Fund. A.R.M. acknowledges funding from UKRI EP/X02878X/1. This publication arises from research funded by the John Fell Oxford University Press (OUP) Research Fund. JFJB acknowledges funding from the UKRI Research Frontier Guarantee program EP/Y014375/1. The authors thank the Editor Mark Dekkers, the Associate Editor Ramon Egli and the two reviewers (Doug Elmore and Roger Fu) for their professional review work and valuable suggestions. The authors also extend their gratitude to the Cyprus Geological Surveying Department for their generous assistance, particularly to Director Christodoulos Hadjigeorgiou, Vasilis Symeou and Nik Papadimitriou.

Data Availability Statement

The measured data relevant to this paper are available in Qi, Muxworthy, Baker et al. (2025); https://doi.org/10.5281/zenodo.15044473.

References

Agrinier, P., & Cannat, M. (1997). Oxygen-isotope constraints on serpentinization processes in ultramafic rocks from the Mid-Atlantic Ridge (23°N). *Proceedings of the ocean drilling program, scientific results* (Vol. 153, pp. 381–388).

Barnes, J. D., Paulick, H., Sharp, Z. D., Bach, W., & Beaudoin, G. (2009). Stable isotope ($\delta^{18}O$, δD, $\delta^{37}Cl$) evidence for multiple fluid histories in mid-Atlantic abyssal peridotites (ODP leg 209). *Lithos*, *110*(1), 83–94. https://doi.org/10.1016/j.lithos.2008.12.004

Barnicoat, A. C., & Cartwright, I. (1995). Focused fluid flow during subduction: Oxygen isotope data from high-pressure ophiolites of the western Alps. *Earth and Planetary Science Letters*, *132*(1), 53–61. https://doi.org/10.1016/0012-821X(95)00040-J

Bassinot, F. C., Labeyrie, L. D., Vincent, E., Quidelleur, X., Shackleton, N. J., & Lancelot, Y. (1994). The astronomical theory of climate and the age of the Brunhes-Matuyama magnetic reversal. *Earth and Planetary Science Letters*, *126*(1–3), 91–108. https://doi.org/10.1016/0012-821X(94)90244-5

Bellon, U. D., Williams, W., Muxworthy, A. R., Souza-Junior, G. F., Nagy, L., Uieda, L., & Trindade, R. I. F. (2025). Efficiency of thermoremanent magnetization acquisition in vortex-state particle assemblies. *Geophysical Research Letters*, *52*(8), e2025GL114771. https://doi.org/10.1029/2025GL114771

Berndt, T., Muxworthy, A. R., & Fabian, K. (2016). Does size matter? Statistical limits of paleomagnetic field reconstruction from small rock specimens. *Journal of Geophysical Research: Solid Earth*, *121*(1), 15–26. https://doi.org/10.1002/2015JB012441

Berndt, T., Ramalho, R. S., Valdez-Grijalva, M. A., & Muxworthy, A. R. (2017). Paleomagnetic field reconstruction from mixtures of titanomagnetites. *Earth and Planetary Science Letters*, *465*, 70–81. https://doi.org/10.1016/j.epsl.2017.02.033

Bersani, D., Andò, S., Vignola, P., Moltifiori, G., Marino, I.-G., Lottici, P. P., & Diella, V. (2009). Micro-Raman spectroscopy as a routine tool for garnet analysis. *Spectrochimica Acta Part A: Molecular and Biomolecular Spectroscopy*, *73*(3), 484–491. https://doi.org/10.1016/j.saa.2008.11.033

Bonnemains, D., Carlut, J., Escartín, J., Mével, C., Andreani, M., & Debret, B. (2016). Magnetic signatures of serpentinization at ophiolite complexes. *Geochemistry, Geophysics, Geosystems*, *17*(8), 2969–2986. https://doi.org/10.1002/2016GC006321

Brenner, A. R., Fu, R. R., Brown, A. J., Hodgin, E. B., Flannery, D. T., & Schmitz, M. D. (2024). Episodic seafloor hydrothermal alteration as a source of stable remagnetizations in Archean volcanic rocks. *Geochemistry, Geophysics, Geosystems*, *25*(12), e2024GC011799. https://doi.org/10.1029/2024GC011799

Brenner, A. R., Fu, R. R., Kylander-Clark, A. R. C., Hudak, G. J., & Foley, B. J. (2022). Plate motion and a dipolar geomagnetic field at 3.25 Ga. *Proceedings of the national academy of sciences* (Vol. 119(44), p. e2210258119). https://doi.org/10.1073/pnas.2210258119

Clube, T. M. M., Creer, K., & Robertson, A. (1985). Palaeorotation of the Troodos microplate, Cyprus. *Nature*, *317*(6037), 522–525. https://doi.org/10.1038/317522a0

Cox, S., Fagereng, Å., & MacLeod, C. J. (2021). Shear zone development in serpentinized mantle: Implications for the strength of oceanic transform faults. *Journal of Geophysical Research: Solid Earth*, *126*(5), e2020JB020763. https://doi.org/10.1029/2020JB020763

Egli, R. (2006). Theoretical aspects of dipolar interactions and their appearance in first-order reversal curves of thermally activated single-domain particles. *Journal of Geophysical Research*, *111*(B12). https://doi.org/10.1029/2006JB004567

Egli, R., Chen, A. P., Winklhofer, M., Kodama, K. P., & Horng, C.-S. (2010). Detection of noninteracting single domain particles using first-order reversal curve diagrams. *Geochemistry, Geophysics, Geosystems*, *11*(1). https://doi.org/10.1029/2009GC002916

Elmore, R. D., Muxworthy, A. R., & Aldana, M. (2012). *Remagnetization and chemical alteration of sedimentary rocks*. (Vol. 371(1), pp. 1–21). The Geological Society of London. https://doi.org/10.1144/sp371.15

Evans, A. D., Standish, C. D., Milton, J. A., Robbins, A. G., Craw, D., Foster, G. L., & Teagle, D. A. H. (2024). Imaging of boron in altered mantle rocks illuminates progressive serpentinisation episodes. *Geochemical Perspectives Letters*, *29*, 20–25. https://doi.org/10.7185/geochemlet.2407

Evans, A. D., Teagle, D. A., Craw, D., Henstock, T. J., & Falcon-Suarez, I. H. (2021). Uplift and exposure of serpentinized massifs: Modeling differential serpentinite diapirism and exhumation of the Troodos Mantle Sequence, Cyprus. *Journal of Geophysical Research: Solid Earth*, *126*(6), e2020JB021079. https://doi.org/10.1029/2020JB021079

Evans, B. W. (2008). Control of the products of serpentinization by the $Fe^{2+}Mg^{-1}$ exchange potential of olivine and orthopyroxene. *Journal of Petrology*, *49*(10), 1873–1887. https://doi.org/10.1093/petrology/egn050

Evans, B. W., Hattori, K., & Baronnet, A. (2013). Serpentinite: What, why, where? *Elements*, *9*(2), 99–106. https://doi.org/10.2113/gselements.9.2.99

Fisher, R. A. (1953). Dispersion on a sphere. *Proceedings of the royal society of London. Series A. Mathematical and physical sciences* (Vol. 217(1130), pp. 295–305). https://doi.org/10.1098/rspa.1953.0064

Frost, B. R., Evans, K. A., Swapp, S. M., Beard, J. S., & Mothersole, F. E. (2013). The process of serpentinization in dunite from New Caledonia. *Lithos*, *178*, 24–39. https://doi.org/10.1016/j.lithos.2013.02.002

Früh-Green, G. L., Plas, A., & Lécuyer, C. (1996). Petrologic and stable isotope constraints on hydrothermal alteration and serpentinization of the EPR Shallow Mantle at Hess Deep (site 895). *Proceedings of the ocean drilling program, scientific results* (Vol. 147). https://doi.org/10.2973/odp.proc.sr.147.016.1996

Fu, R. R., Lima, E. A., Volk, M. W., & Trubko, R. (2020). High-sensitivity moment magnetometry with the quantum diamond microscope. *Geochemistry, Geophysics, Geosystems*, *21*(8), e2020GC009147. https://doi.org/10.1029/2020GC009147

Fu, R. R., Volk, M. W. R., Bilardello, D., Libourel, G., Lesur, G. R. J., & Ben Dor, O. (2021). The fine-scale magnetic history of the Allende Meteorite: Implications for the structure of the Solar Nebula. *AGU Advances*, *2*(3), e2021AV000486. https://doi.org/10.1029/2021AV000486

Fu, R. R., Weiss, B. P., Lima, E. A., Kehayias, P., Araujo, J. F., Glenn, D. R., et al. (2017). Evaluating the paleomagnetic potential of single zircon crystals using the Bishop Tuff. *Earth and Planetary Science Letters*, *458*, 1–13. https://doi.org/10.1016/j.epsl.2016.09.038

Gass, I. (1968). Is the Troodos massif of Cyprus a fragment of Mesozoic ocean floor? *Nature*, *220*(5162), 39–42. https://doi.org/10.1038/220039a0

Gass, I. G. (1977). Origin and emplacement of ophiolites. *Geological Society*, *7*(1), 72–76. https://doi.org/10.1144/GSL.SP.1977.007.01.07

Gass, I. G., & Masson-Smith, D. (1963). The geology and gravity anomalies of the Troodos Massif, Cyprus. *Philosophical Transactions of the Royal Society of London - Series A: Mathematical and Physical Sciences*, *255*(1060), 417–467. https://doi.org/10.1098/rsta.1963.0009

George, R. P., Jr. (1978). Structural petrology of the Olympus ultramafic complex in the Troodos ophiolite, Cyprus. *GSA Bulletin*, *89*(6), 845–865. https://doi.org/10.1130/0016-7606(1978)89<845:Spotou>2.0.Co;2

Glenn, D. R., Fu, R. R., Kehayias, P., Le Sage, D., Lima, E. A., Weiss, B. P., & Walsworth, R. L. (2017). Micrometer-scale magnetic imaging of geological samples using a quantum diamond microscope. *Geochemistry, Geophysics, Geosystems*, *18*(8), 3254–3267. https://doi.org/10.1002/2017GC006946

Glenn, D. R., Lee, K., Park, H., Weissleder, R., Yacoby, A., Lukin, M. D., et al. (2015). Single-cell magnetic imaging using a quantum diamond microscope. *Nature Methods*, *12*(8), 736–738. https://doi.org/10.1038/nmeth.3449

Granot, R., Abelson, M., Ron, H., & Agnon, A. (2006). The oceanic crust in 3D: Paleomagnetic reconstruction in the Troodos ophiolite gabbro. *Earth and Planetary Science Letters*, *251*(3–4), 280–292. https://doi.org/10.1016/j.epsl.2006.09.019

Greenbaum, D. (1972). Magmatic processes at ocean ridges: Evidence from the Troodos massif, Cyprus. *Nature; Physical Science*, *238*(80), 18–21. https://doi.org/10.1038/physci238018a0

Guillot, S., Schwartz, S., Reynard, B., Agard, P., & Prigent, C. (2015). Tectonic significance of serpentinites. *Tectonophysics*, *646*, 1–19. https://doi.org/10.1016/j.tecto.2015.01.020

Harrison, R. J., & Feinberg, J. M. (2008). FORCinel: An improved algorithm for calculating first-order reversal curve distributions using locally weighted regression smoothing. *Geochemistry, Geophysics, Geosystems*, *9*(5). https://doi.org/10.1029/2008GC001987

Hurst, S. D., Moores, E. M., & Varga, R. J. (1994). Structural and geophysical expression of the solea graben, Troodos Ophiolite, Cyprus. *Tectonics*, *13*(1), 139–156. https://doi.org/10.1029/93TC02066

Klein, F., Bach, W., Humphris, S. E., Kahl, W.-A., Jöns, N., Moskowitz, B., & Berquó, T. S. (2014). Magnetite in seafloor serpentinite: Some like it hot. *Geology*, *42*(2), 135–138. https://doi.org/10.1130/G35068.1

Levine, E. V., Turner, M. J., Kehayias, P., Hart, C. A., Langellier, N., Trubko, R., et al. (2019). Principles and techniques of the quantum diamond microscope. *Nanophotonics*, *8*(11), 1945–1973. https://doi.org/10.1515/nanoph-2019-0209

Lurcock, P. C., & Wilson, G. S. (2012). PuffinPlot: A versatile, user-friendly program for paleomagnetic analysis. *Geochemistry, Geophysics, Geosystems*, *13*(6). https://doi.org/10.1029/2012gc004098

MacLeod, C. J., Allerton, S., Gass, I., & Xenophontos, C. (1990). Structure of a fossil ridge-transform intersection in the Troodos ophiolite. *Nature*, *348*(6303), 717–720. https://doi.org/10.1038/348717a0

McCallum, J. E. (1989). *Sedimentation and tectonics of the Plio-Pleistocene of Cyprus. (PhD)*. University of Edinburgh.

Merry, T. A. J. (2022). *Upper mantle seismic anisotropy in the eastern Mediterranean and seismicity in Cyprus. (PhD)*. Imperial College London. Retrieved from http://hdl.handle.net/10044/1/101422

Morris, A. (1996). *A review of palaeomagnetic research in the Troodos ophiolite*. (Vol. 105(1), pp. 311–324). Geological Society, London, Special Publications. https://doi.org/10.1144/gsl.sp.1996.105.01.27

Mukasa, S. B., & Ludden, J. N. (1987). Uranium-lead isotopic ages of plagiogranites from the Troodos ophiolite, Cyprus, and their tectonic significance. *Geology*, *15*(9), 825–828. https://doi.org/10.1130/0091-7613(1987)15<825:Uiaopf>2.0.Co;2

Muxworthy, A., & Williams, W. (2005). Magnetostatic interaction fields in first-order-reversal-curve diagrams. *Journal of Applied Physics*, *97*(6), 063905. https://doi.org/10.1063/1.1861518

Muxworthy, A. R., Turney, J. N., Qi, L., Baker, E. B., Perkins, J. R., & Abdulkarim, M. A. (2023). Interpreting high-temperature magnetic susceptibility data of natural systems. *Frontiers in Earth Science*, *11*, Review. https://doi.org/10.3389/feart.2023.1171200

Muxworthy, A. R., & Williams, W. (2006). Critical single-domain/multidomain grain sizes in noninteracting and interacting elongated magnetite particles: Implications for magnetosomes. *Journal of Geophysical Research*, *111*(B12). https://doi.org/10.1029/2006JB004588

Nagy, L., Moreno, R., Muxworthy, A. R., Williams, W., Paterson, G. A., Tauxe, L., & Valdez-Grijalva, M. A. (2024). Micromagnetic determination of the FORC response of paleomagnetically significant magnetite assemblages. *Geochemistry, Geophysics, Geosystems*, *25*(7), e2024GC011465. https://doi.org/10.1029/2024GC011465

Nichols, C. I. O., Bryson, J. F. J., Cottrell, R. D., Fu, R. R., Harrison, R. J., Herrero-Albillos, J., et al. (2021). A time-resolved paleomagnetic record of main group pallasites: Evidence for a large-cored, thin-mantled parent body. *Journal of Geophysical Research: Planets*, *126*(7), e2021JE006900. https://doi.org/10.1029/2021JE006900

Notini, L., Scambelluri, M., Tommasi, A., Zanetti, A., Ferri, F., Rodríguez-Vargas, A., & Rampone, E. (2024). Probing the deep mantle wedge in an active subduction zone: Xenoliths from the Mercaderes Volcanic District, Southern Colombia. *Lithos*, *464–465*, 107401. https://doi.org/10.1016/j.lithos.2023.107401

Nuriel, P., Katzir, Y., Abelson, M., Valley, J. W., Matthews, A., Spicuzza, M. J., & Ayalon, A. (2009). Fault-related oceanic serpentinization in the Troodos ophiolite, Cyprus: Implications for a fossil oceanic core complex. *Earth and Planetary Science Letters*, *282*(1–4), 34–46. https://doi.org/10.1016/j.epsl.2009.02.029

Pei, Z., Williams, W., Nagy, L., Paterson, G. A., Moreno, R., Muxworthy, A. R., & Chang, L. (2025). FORCINN: First-order reversal curve inversion of magnetite using neural networks. *Geophysical Research Letters*, *52*(3), e2024GL112769. https://doi.org/10.1029/2024GL112769

Poole, A., & Robertson, A. (1998). Pleistocene fanglomerate deposition related to uplift of the Troodos Ophiolite, Cyprus. *Proceedings of the ocean drilling program, scientific results* (Vol. 160). https://doi.org/10.2973/odp.proc.sr.160.064.1998

Qi, L., Allerton, S., Muxworthy, A. R., Zhang, Y., & Gergov, H. (2025). Remagnetization of serpentinite during deformation: Evidence from a fossil oceanic transform fault zone of the Troodos ophiolite. *Journal of Geophysical Research: Solid Earth*, *130*(4), e2024JB030790. https://doi.org/10.1029/2024JB030790

Qi, L., Muxworthy, A. R., Baker, E. B., Cao, X., Allerton, S., Bryson, J. F. J., & Zhang, Y. (2025). Quantum diamond microscope dataset for serpentinite from the Troodos ophiolite and oxygen isotope measurements [Dataset]. *Zenodo*. https://doi.org/10.5281/zenodo.15044473

Qi, L., Muxworthy, A. R., Collier, J. S., & Allerton, S. (2025). Magnetization of ultramafic rocks in the Troodos ophiolite: Implications for ridge axis serpentinization and ophiolite emplacement. *Journal of Geophysical Research: Solid Earth*, *130*(4), e2024JB030452. https://doi.org/10.1029/2024JB030452

Roberts, A. P., Heslop, D., Zhao, X., & Pike, C. R. (2014). Understanding fine magnetic particle systems through use of first-order reversal curve diagrams. *Reviews of Geophysics*, *52*(4), 557–602. https://doi.org/10.1002/2014RG000462

Roberts, A. P., Pike, C. R., & Verosub, K. L. (2000). First-order reversal curve diagrams: A new tool for characterizing the magnetic properties of natural samples. *Journal of Geophysical Research*, *105*(B12), 28461–28475. https://doi.org/10.1029/2000JB900326

Robertson, A. H. (1998). Tectonic significance of the Eratosthenes Seamount: A continental fragment in the process of collision with a subduction zone in the eastern Mediterranean (Ocean drilling program leg 160). *Tectonophysics*, *298*(1–3), 63–82. https://doi.org/10.1016/S0040-1951(98)00178-4

Rooney, J. S., Tarling, M. S., Smith, S. A. F., & Gordon, K. C. (2018). Submicron Raman spectroscopy mapping of serpentinite fault rocks. *Journal of Raman Spectroscopy*, *49*(2), 279–286. https://doi.org/10.1002/jrs.5277

Saccocia, P. J., Seewald, J. S., & Shanks, W. C. (2009). Oxygen and hydrogen isotope fractionation in serpentine–water and talc–water systems from 250 to 450°C, 50 MPa. *Geochimica et Cosmochimica Acta*, *73*(22), 6789–6804. https://doi.org/10.1016/j.gca.2009.07.036

Shebanova, O. N., & Lazor, P. (2003). Raman spectroscopic study of magnetite (FeFe2O4): A new assignment for the vibrational spectrum. *Journal of Solid State Chemistry*, *174*(2), 424–430. https://doi.org/10.1016/S0022-4596(03)00294-9

Shelton, A. (1993). *Troodos revisited: The mount Olympus gravity anomaly*. (Vol. 76(1), pp. 197–212). Geological Society. https://doi.org/10.1144/GSL.SP.1993.076.01.09

Skelton, A. D. L., & Valley, J. W. (2000). The relative timing of serpentinisation and mantle exhumation at the ocean-continent transition, Iberia: Constraints from oxygen isotopes. *Earth and Planetary Science Letters*, *178*(3), 327–338. https://doi.org/10.1016/S0012-821X(00)00087-X

Souza-Junior, G. F., Uieda, L., Trindade, R. I. F., Carmo, J., & Fu, R. (2024). Full vector inversion of magnetic microscopy images using Euler deconvolution as prior information. *Geochemistry, Geophysics, Geosystems*, *25*(7), e2023GC011082. https://doi.org/10.1029/2023GC011082

Steele, S. C., Fu, R. R., Volk, M. W. R., North, T. L., Brenner, A. R., Muxworthy, A. R., et al. (2023). Paleomagnetic evidence for a long-lived, potentially reversing Martian dynamo at ~3.9 Ga. *Science Advances*, *9*(21), eade9071. https://doi.org/10.1126/sciadv.ade9071

Tang, F., Taylor, R. J. M., Einsle, J. F., Borlina, C. S., Fu, R. R., Weiss, B. P., et al. (2019). Secondary magnetite in ancient zircon precludes analysis of a Hadean geodynamo. *Proceedings of the national academy of sciences* (Vol. 116(2), pp. 407–412). https://doi.org/10.1073/pnas.1811074116

Tarling, M. S., Rooney, J. S., Viti, C., Smith, S. A. F., & Gordon, K. C. (2018). Distinguishing the Raman spectrum of polygonal serpentine. *Journal of Raman Spectroscopy*, *49*(12), 1978–1984. https://doi.org/10.1002/jrs.5475

Thallner, D., Biggin, A. J., McCausland, P. J. A., & Fu, R. R. (2021). New paleointensities from the Skinner Cove Formation, Newfoundland, suggest a changing state of the geomagnetic field at the Ediacaran-Cambrian transition. *Journal of Geophysical Research: Solid Earth*, *126*(9), e2021JB022292. https://doi.org/10.1029/2021JB022292

Thy, P. (1987). Petrogenetic implications of mineral crystallization trends of Troodos cumulates, Cyprus. *Geological Magazine*, *124*(1), 1–11. https://doi.org/10.1017/S0016756800015739

Vine, F., Poster, C., & Gass, I. (1973). Aeromagnetic survey of the Troodos igneous massif, Cyprus. *Nature; Physical Science*, *244*(133), 34–38. https://doi.org/10.1038/physci244034a0

Volk, M. W. R., Fu, R. R., Mittelholz, A., & Day, J. M. D. (2021). Paleointensity and rock magnetism of Martian Nakhlite Meteorite miller range 03346: Evidence for intense small-scale crustal magnetization on Mars. *Journal of Geophysical Research: Planets*, *126*(5), e2021JE006856. https://doi.org/10.1029/2021JE006856

Volk, M. W. R., Fu, R. R., Trubko, R., Kehayias, P., Glenn, D. R., & Lima, E. A. (2022). QDMlab: A MATLAB toolbox for analyzing Quantum Diamond Microscope (QDM) magnetic field maps. *Computers and Geosciences*, *167*, 105198. https://doi.org/10.1016/j.cageo.2022.105198

Watson, G. S. (1983). Large sample theory of the langevin distribution. *Journal of Statistical Planning and Inference*, *8*(3), 245–256. https://doi.org/10.1016/0378-3758(83)90043-5

Weiss, B. P., Fu, R. R., Einsle, J. F., Glenn, D. R., Kehayias, P., Bell, E. A., et al. (2018). Secondary magnetic inclusions in detrital zircons from the Jack Hills, Western Australia, and implications for the origin of the geodynamo. *Geology*, *46*(5), 427–430. https://doi.org/10.1130/G39938.1

Wenner, D. B., & Taylor, H. P. (1971). Temperatures of serpentinization of ultramafic rocks based on O^{18}/O^{16} fractionation between coexisting serpentine and magnetite. *Contributions to Mineralogy and Petrology*, *32*(3), 165–185. https://doi.org/10.1007/BF00643332

Wilson, R. A. M., & Ingham, F. T. (1959). *The geology of the Xeros-Troodos area with an account of the mineral resources* (Vol. 1(1), pp. 1–184). Geological Survey Department of Cyprus, Memoir.

Yuan, X., & Mayanovic, R. A. (2017). An empirical study on Raman peak fitting and its application to Raman quantitative research. *Applied Spectroscopy*, *71*(10), 2325–2338. https://doi.org/10.1177/0003702817721527

Zheng, Y.-F. (1993). Calculation of oxygen isotope fractionation in hydroxyl-bearing silicates. *Earth and Planetary Science Letters*, *120*(3), 247–263. https://doi.org/10.1016/0012-821X(93)90243-3